Pergamon

Acta mater. Vol. 46, No. 11, pp. 3915–3928, 1998

Printed in Great Britain

PII: S1359-6454(98)00058-5

1359-6454/98 $19.00 + 0.00

COMPUTER SIMULATION OF MORPHOLOGICAL EVOLUTION AND COARSENING KINETICS OF δ' (Al_3Li) PRECIPITATES IN Al–Li ALLOYS

R. PODURI and L.-Q. CHEN†

Department of Materials Science and Engineering, The Pennsylvania State University, University Park, PA 16802-5006, U.S.A.

(Received 5 January 1997; accepted 7 February 1998)

Abstract—The morphological evolution and coarsening kinetics of $L1_2$ ordered (Al_3Li) precipitates (δ') in a f.c.c. disordered matrix (α) were investigated using computer simulations based on microscopic diffusion equations. The effective interatomic interactions were fitted to the phase diagram using a two-neighbor mean-field model whereas the kinetic parameter in the microscopic diffusion equation was fitted to the chemical diffusion coefficient in the equilibrium disordered phase. The coalescence or encounter among precipitates which belong to any one of the four different antiphase domains of the $L1_2$ ordered phase is automatically taken into account. Volume fractions ranging from 20 to 65% were studied. Structure, scaling and particle-size distribution (PSD) functions were calculated. It is shown that the PSDs become increasingly broad and their skewness changes sign from negative to positive with increasing precipitate volume fraction. It is found that the cube of the average particle radius varies approximately linearly with time in the scaling regime for all the volume fractions studied, with the rate constant increasing with volume fraction. During coarsening, the volume fraction is not constant, approaching the equilibrium value asymptotically with time. The results are compared with existing analytical theories and experimental measurements.

1. INTRODUCTION

In general, precipitation of second-phase particles from a given matrix can be characterized by two stages. The first stage involves phase transformations, driven by the reduction in the bulk free energies. They may take place either by a nucleation-and-growth mechanism if the parent phase is metastable, or by a continuous mechanism if the matrix is unstable, with respect to its transformation to the precipitate phase. The second stage involves the coarsening of precipitate particles, driven by the reduction in the total interfacial energies between precipitates and matrix. During coarsening, the volume fraction of the precipitate phase is close to the equilibrium value determined from the lever rule. In recent works, the phase transformation paths leading to the precipitation of δ' (Al_3Li) ordered particles from a disordered matrix (α) in Al–Li alloys using microscopic Langevin diffusion equations were studied [1]. In this paper, attention is focused on the coarsening kinetics of δ' particles after phase transformations.

The first formal theory of coarsening was developed more than 30 years ago by Lifshitz and Slyozov [2], and Wagner [3], i.e. the so-called LSW theory which predicts that the cube of average particle size, $\langle R\rangle$, is linearly proportional to time t, i.e. $\langle R\rangle^3 = Kt$, where K is the rate constant, and the particle sizes normalized by the average size have a unique distribution which is independent of time. LSW theory assumes that precipitates are spherical and the particle density is very low so that the typical interparticle distance is large compared to the average size. Coarsening of real alloy systems, however, is complicated by many other factors including the finite volume-fraction, nonspherical shapes of particles, the elastic interactions between precipitates, and applied load. Therefore, there have been many attempts to modify the LSW theory by taking into account some of the factors, in particular the effect of volume fraction, as summarized in a number of review articles (see, e.g. Ref. [4]). Examples of these attempts include those of Ardell [4], Tsumuraya and Miyata [5], Asimov [6], Sarian and Weart [7], and Aubauer [8] by solving the diffusion equation using more realistic diffusion geometry, and those of Brailsford and Wynblatt [9], Voorhees and Glicksman [10], Marqusee and Ross [11], Tokuyama and Kawasaki [12], and Marsh and Glicksman [13] by using statistical approaches. Davies *et al.* [14] developed the so-called Lifshitz–Slyozov encounter modified (LSEM) theory by taking into account the effect of particle coalescence or encounter through the addition of a source term to the continuity equation for the PSDs. Despite these advances, in general, the agreement between theoretically predicted and experimentally measured

†To whom all correspondence should be addressed.

volume-fraction dependence of PSDs and the rate constant in the cubic growth law is not satisfactory.

The $\delta' + \alpha$ two-phase alloy in Al–Li is a relatively simple system for studying coarsening kinetics because δ' particles have a very small lattice mismatch with the matrix, and thus there is a negligible elastic strain energy contribution to coarsening. Most experimental studies showed that the average radius, $\langle R \rangle$, of δ' particles as a function of time, t, follows the cubic law, consistent with the classical LSW theory and its later modifications. However, there is still no single theory which can satisfactorily describe all aspects of coarsening. For example, Mahalingam *et al.* [15] conducted a systematic study of the coarsening kinetics of δ' precipitates up to a volume fraction of 0.55 and found good agreement between the measured PSDs and those predicted by the LSEM model of Davies *et al.* [14], after appropriately normalizing the theoretically predicted curves. However, the variation of the rate constant with volume fraction was found to be closer to that predicted by Ardell's modified Lifshitz–Slyozov–Wagner (MLSW) theory [16]. More recently, Kamio and Sato [17] conducted a similar study on the coarsening kinetics of δ' precipitates, and found that at low volume fractions ($< 30\%$), the variation of the rate constant with volume fraction was closest to that predicted by the LSEM model, while an inspection of their PSDs shows that they are better described by Ardell's MLSW theory.

In recent years, there has been increasing interest in using computer simulations to study coarsening kinetics. Computer simulations could be the ultimate bridge between theories and experimental observations. On the one hand, systems in a computer simulation can be made sufficiently simple to allow direct comparison with analytical theories; and on the other hand, it is now possible to include many of the factors which affect coarsening in a computer simulation and therefore to make direct contacts with experiments. Most of the previous computer simulations employed either the sharp-interface front-tracking model for directly solving the diffusion equations in a system with many coarsening particles or the diffuse-interface model through the numerical solution of Cahn–Hilliard equations. The main limitation of the front-tracking model is due to the moving boundary problem, although a recent work using a multipole method was able to simulate volume fractions of the precipitate phase as high as 40% in two dimensions (2D) [18]. Moreover, it does not take into account the coalescence, which becomes increasingly frequent with increasing volume fraction. The Cahn–Hilliard equation is basically a nonlinear diffusion equation which was initially applied to study the kinetics of spinodal decomposition. Since it is a diffusion equation, it also automatically describes the coarsening process after spinodal decomposition. One of the advantages of the Cahn–Hilliard equation over sharp-interface approaches is the avoidance of the moving boundary problem. The position of boundaries is specified by locations at which the values of the concentration are between that corresponding to the precipitate phase and that corresponding to the matrix phase. However, when the volume fraction of the precipitate phase increases above the percolation limit, the particles coalesce and both phases become interconnected. Therefore, it cannot be directly applied to modeling the kinetics of coarsening in $\delta' + \alpha$ two-phase alloys in which the precipitate phase is dispersed even if the volume fraction is above 50%.

This paper employs a computer simulation approach based on the microscopic diffusion equations [19] to model the coarsening behavior of δ' particles in a disordered Al–Li matrix. The model can be applied to all stages of the precipitation process including nucleation, growth and coarsening [20]. It can describe simultaneously atomic ordering and compositional phase separation and allows arbitrary morphologies [20]. Elastic energy contribution to the morphological evolution and coarsening can also be incorporated [21, 22]. More importantly, the effect of volume fraction, the coalescence of two in-phase ordered particles to form a larger one, or the separation of two close-by out-of-phase particles by the disordered matrix, are automatically taken into account. An alternative to using the microscopic diffusion equations is to employ the continuum diffuse-interface field kinetic model [23, 24] by using a three-component long-range order field and a composition field to describe the structure and composition of the $L1_2$ ordered domains [25, 26]. It is a continuation of the systematic investigation on the early stages of the precipitation process of ordered δ' particles from a disordered matrix [1, 27]. As a first attempt, a projected 2D model from a three-dimensional (3D) f.c.c. lattice was employed, i.e. all the interatomic interactions were taken into account in 3D, although the simulations were performed on the project 2D square lattice of a 3D f.c.c. lattice. The structure and scaling function, as well as the PSDs and their skewness, are analyzed from the simulated two-phase microstructures as a function of time up to a volume fraction of 0.65 of the δ' phase. In particular, it will be demonstrated that as the volume fraction increases, the rate constant increases, the PSDs become increasingly broad, and the skewness of the PSDs changes sign from negative to positive. The results on the coarsening kinetics of $L1_2$ ordered precipitates obtained from the computer simulations were compared with existing theoretical models and experimental measurements.

2. THE COMPUTER SIMULATION MODEL

2.1. Microscopic diffusion equations

In this study, the morphology of a two-phase alloy is described by a single-site occupation probability function, $P(\mathbf{r},t)$, which is the probability that a given lattice site, $\mathbf{r}$, is occupied by a solute atom (e.g. Li in Al–Li alloys), at a given time t. The rates of change of these probabilities are then described by the Önsager-type diffusion equations as being linearly proportional to the thermodynamic driving force [19]

$$\frac{\mathrm{d}P(\mathbf{r},t)}{\mathrm{d}t}=\frac{C_\mathrm{o}(1-C_\mathrm{o})}{k_\mathrm{B}T}\sum_{\mathbf{r}'}L(\mathbf{r}-\mathbf{r}')\frac{\partial F}{\partial P(\mathbf{r}',t)} \quad (1)$$

where the summation is carried out over all N crystal lattice sites of a system, $L(\mathbf{r}-\mathbf{r}')$ is the proportionality constant which is related to the probability of an elementary diffusion jump from site $\mathbf{r}$ to $\mathbf{r}'$, per unit of time, T the temperature, k_B the Boltzmann constant, C_o the overall solute composition, and F the total free energy of the system, which is a function of the single-site occupation probability function.

Since the total number of atoms is conserved, the sum of the single-site occupation probabilities over all the lattice sites is equal to the total number of solute atoms in the system

$$\sum_{r=1}^{N}P(\mathbf{r},t)=C_\mathrm{o}N.$$

Summing both sides of equation (1) over all atomic sites $\mathbf{r}$ and using the fact that the total number of solute atoms is a constant, gives the following identity:

$$\sum_{\mathbf{r}}L(\mathbf{r})\sum_{\mathbf{r}'}\frac{\partial F}{\partial P(\mathbf{r}',t)}=0. \quad (2)$$

Since the second summation in equation (2) is nonzero for nonequilibrium systems, the conservation condition for the total number of atoms requires that the first term be zero, i.e.

$$\sum_{\mathbf{r}}L(\mathbf{r})=0. \quad (3)$$

2.2. Microscopic Langevin equations

It is easy to see that kinetic equation (1) is deterministic and hence cannot describe processes which require thermal fluctuations, such as nucleation. Therefore, in order to study the coarsening behavior over a wide range of volume fractions, including the region of the two-phase field where δ' precipitates formed by a nucleation and growth mechanism, a random noise term, $\xi(\mathbf{r},t)$, was introduced to the kinetic equation (1) to simulate the thermal fluctuations

$$\frac{\mathrm{d}P(\mathbf{r},t)}{\mathrm{d}t}=\frac{C_\mathrm{o}(1-C_\mathrm{o})}{k_\mathrm{B}T}\sum_{\mathbf{r}'}L(\mathbf{r}-\mathbf{r}')\frac{\partial F}{\partial P(\mathbf{r}',t)}+\xi(\mathbf{r},t) \quad (4)$$

where $\xi(\mathbf{r},t)$ is assumed to be Gaussian-distributed with average zero and uncorrelated with respect to both space and time, i.e. it obeys the so-called fluctuation dissipation theorem [28]

$$\langle\xi(\mathbf{r},t)\rangle=0$$
$$\langle\xi(\mathbf{r},t)\xi(\mathbf{r}',t')\rangle=-2k_\mathrm{B}TL(\mathbf{r}-\mathbf{r}')\delta(t-t')\delta(\mathbf{r}-\mathbf{r}') \quad (5)$$

where angular brackets denote averaging, $\langle\xi(\mathbf{r},t)\rangle$ is the average value of the noise over space and time, $\langle\xi(\mathbf{r},t)\xi(\mathbf{r}',t')\rangle$ the correlation, and δ the Kronecker delta function. The noise term is similar to that introduced by Cook to the Cahn–Hilliard equation [29]. With the noise term, equation (4) becomes stochastic and is, in fact, the microscopic version of the continuum Langevin equation [30].

2.3. Microscopic Langevin equation in Fourier space

With the equations describing the evolution of real-space single-site occupation probability distribution function $P(\mathbf{r},t)$, the corresponding growth rates of the amplitudes of composition modulations, $\tilde{P}(\mathbf{k},t)$, at a given wave vector, $\mathbf{k}$, can be easily obtained by taking the Fourier transform of equation (4), i.e.

$$\frac{\mathrm{d}\tilde{P}(\mathbf{k},t)}{\mathrm{d}t}=\frac{C_\mathrm{o}(1-C_\mathrm{o})}{k_\mathrm{B}T}\tilde{L}(\mathbf{k})\left\{\frac{\partial F}{\partial P(\mathbf{r},t)}\right\}_{\mathbf{k}}+\xi(\mathbf{k},t) \quad (6)$$

where $\tilde{P}(\mathbf{k},t)$, $\tilde{L}(\mathbf{k})$, $\{\partial F/\partial P(\mathbf{r},t)\}_{\mathbf{k}}$, and $\xi(\mathbf{k},t)$ are the Fourier transforms of $P(\mathbf{r},t)$, $L(\mathbf{r})$, $\partial F/\partial P(\mathbf{r},t)$, and $\xi(\mathbf{r},t)$, respectively. For example

$$\tilde{P}(\mathbf{k},t)=\sum_{\mathbf{r}}P(\mathbf{r},t)\exp(-\mathrm{i}\mathbf{k}\mathbf{r}).$$

Since

$$\tilde{L}(\mathbf{k}=0)=\tilde{L}(0)=\sum_{\mathbf{r}}L(\mathbf{r})$$

the conservation condition [equation (3)] in the reciprocal space becomes

$$\tilde{L}(0)=0. \quad (7)$$

2.4. Application to a f.c.c. lattice

In the mean-field approximation, the total free energy of a system is given by

$$F=\frac{1}{2}\sum_{\mathbf{r}}\sum_{\mathbf{r}'}W(\mathbf{r}-\mathbf{r}')P(\mathbf{r})P(\mathbf{r}')+k_\mathrm{B}T\sum_{\mathbf{r}}\left[P(\mathbf{r})\ln P(\mathbf{r})+\big(1-P(\mathbf{r})\big)\ln\big(1-P(\mathbf{r})\big)\right] \quad (8)$$

where $W(\mathbf{r}-\mathbf{r}')$ is the effective interchange energy given as the sum of the A–A and B–B pairwise interaction energies, minus twice the A–B pairwise interaction energy

$$W(\mathbf{r}-\mathbf{r}') = W_{AA}(\mathbf{r}-\mathbf{r}') + W_{BB}(\mathbf{r}-\mathbf{r}') - 2W_{AB}(\mathbf{r}-\mathbf{r}'). \quad (9)$$

Although it has been well known that, for a f.c.c. lattice, the above mean field free energy incorrectly gives a second-order order–disorder phase transition at composition $C = 0.5$ where it is supposed to be first order, yet with the proper choice of W_1 and W_2, it can provide a reasonably good approximation of the low-temperature two-phase ($\alpha + \delta'$) field [31]. Moreover, a more accurate free energy density function is not expected to significantly change the coarsening kinetics as along as it provides the appropriate interfacial energy and the thermodynamic factor in the chemical diffusion coefficient.

Using equations (8) and (6)

$$\frac{d\tilde{P}(\mathbf{k},t)}{dt} = \frac{C_o(1-C_o)}{k_B T} L(\mathbf{k}) \left\{ \tilde{V}(\mathbf{k})\tilde{P}(\mathbf{k},t) + k_B T \left[\ln\left(\frac{P(\mathbf{r},t)}{1-P(\mathbf{r},t)} \right) \right]_{\mathbf{k}} \right\} + \xi(\mathbf{k},t) \quad (10)$$

in which $\tilde{V}(\mathbf{k})$ is the Fourier transform of $W(\mathbf{r})$, and for a f.c.c. lattice, is given by

$$\tilde{V}(\mathbf{k}) = 4W_1(\cos\pi h \cdot \cos\pi k + \cos\pi h \cdot \cos\pi l + \cos\pi k \cdot \cos\pi l) + 2W_2(\cos 2\pi h + \cos 2\pi k + \cos 2\pi l) + \cdots \quad (11)$$

where W_1 and W_2 are the first-nearest and second-nearest neighbor effective interchange energies, respectively, and h, k, and l are related to the reciprocal lattice through

$$\mathbf{k} = (k_x, k_y, k_z) = 2\pi(h\mathbf{a}_1^* + k\mathbf{a}_2^* + l\mathbf{a}_3^*)$$

with $\mathbf{a}_1^*$, $\mathbf{a}_2^*$ and $\mathbf{a}_3^*$ being the unit reciprocal lattice vectors of the f.c.c. lattice along [100], [010], and [001] directions, respectively, and $|\mathbf{a}_1^*| = |\mathbf{a}_2^*| = |\mathbf{a}_3^*| = 1/a_o$ (a_o is the lattice parameter of the f.c.c. lattice).

By assuming atomic jumps between nearest neighbor sites only and using the condition that the total number of atoms in the system are conserved [equation (7)], for a f.c.c. lattice, the following equation can be written [19]

$$\tilde{L}(\mathbf{k}) = -4L_1[3 - \cos\pi h \cdot \cos\pi k - \cos\pi k \cdot \cos\pi l - \cos\pi l \cdot \cos\pi h] \quad (12)$$

where L_1 is proportional to the jump probability between the nearest-neighbor sites at a time unit.

2.5. 2D approximation of a 3D problem [1]

Although it is straightforward and desirable to perform 3D simulations using the microscopic diffusion equations outlined above, a 2D simulation is much less computationally intensive, and the analysis and visualization of the atomic configuration and multiphase morphologies are much easier. As a result, all the results reported in this paper were obtained using 2D projections of a 3D system. It is equivalent to assuming that the occupation probabilities do not depend on the coordinate z along the [001] axis. The $L1_2$ ordered structure of the δ' particles and its projection are shown in Fig. 1.

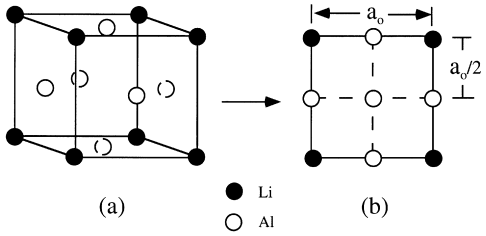

Fig. 1. (a) $L1_2$ unit cell. (b) The projection of the $L1_2$ unit cell.

The 2D projection of a f.c.c. lattice along the [001] direction, is a square lattice whose lattice parameter is half of that of the f.c.c. lattice. Therefore, a lattice vector $\mathbf{r}$ in the 2D square lattice can be written as

$$\mathbf{r} = x'\mathbf{b}_1 + y'\mathbf{b}_2 = \frac{x'}{2}\mathbf{a}_1 + \frac{y'}{2}\mathbf{a}_2$$

where $\mathbf{b}_1$ and $\mathbf{b}_2$ are the unit cell vectors of the square lattice, and $\mathbf{a}_1$ and $\mathbf{a}_2$ are the unit cell vectors of the f.c.c. lattice on the projected plane. The corresponding reciprocal lattice vector $\mathbf{k}$ for the square lattice is

$$\mathbf{k}' = 2\pi(h'\mathbf{b}_1^* + k'\mathbf{b}_2^*) = 2\pi(2h'\mathbf{a}_1^* + 2k'\mathbf{a}_2^*)$$

where $\mathbf{b}_1^*$ and $\mathbf{b}_2^*$ are corresponding reciprocal unit cell vectors for the square lattice, and $\mathbf{a}_1^*$ and $\mathbf{a}_2^*$ are the reciprocal unit cell vectors for the lattice defined by the real space unit cell vectors, $\mathbf{a}_1$ and $\mathbf{a}_2$.

Therefore, on the projected 2D square lattice, the kinetic equation in the reciprocal space is given by

$$\frac{d\tilde{P}(\mathbf{k}',t)}{dt} = \frac{C_o(1-C_o)}{k_B T} L(\mathbf{k}') \left\{ \tilde{V}(\mathbf{k}')\tilde{P}(\mathbf{k}',t) + k_B T \left[\ln\left(\frac{P(\mathbf{r},t)}{1-P(\mathbf{r},t)} \right) \right]_{\mathbf{k}'} \right\} + \xi(\mathbf{k}',t) \quad (13)$$

with

$$\tilde{V}(\mathbf{k}') = 4W_1(\cos 2\pi h' \cdot \cos 2\pi k' + \cos 2\pi h' + \cos 2\pi k') + 2W_2(\cos 4\pi h' + \cos 4\pi k' + 1) + \cdots \quad (14)$$

and

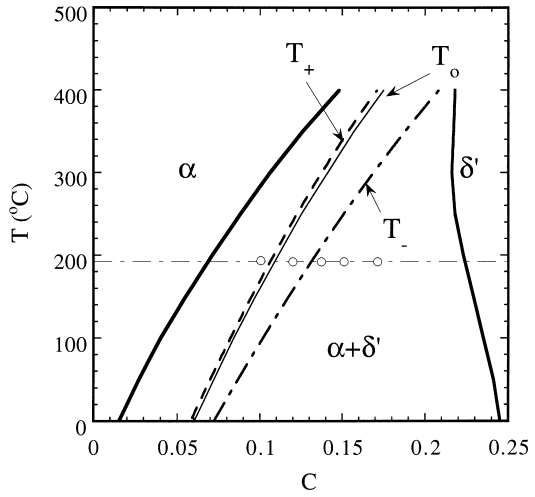

Fig. 2. The computed Al–Li phase diagram with a two-neighbor mean-field model. The labels for the different lines in the diagram are explained in the text.

$$\tilde{L}(\mathbf{k}') = -4L_1\left[3 - \cos 2\pi h' \cdot \cos 2\pi k' - \cos 2\pi k' - \cos 2\pi h'\right]. \quad (15)$$

2.6. Numerical solution to the kinetic equations

Numerically, a simple Euler technique was used to solve the microscopic Langevin equations in the reciprocal space [equation (3)]. The real space probabilities are then recovered by back Fourier transforms. Following the spatial distribution of these probabilities with time yields all the information concerning the dynamics of atomic and morphological evolution along a transformation path including order → disorder, compositional clustering, and coarsening.

2.7. Generation of thermal noise

To generate random numbers which satisfy the fluctuation-dissipation theorem, first, a random number, μ, is generated at any given lattice point at a given time step from a normal distribution, a Gaussian with average 0.0 and standard deviation 1.0. The Fourier transform of the random numbers are then multiplied by a factor to obtain the desired variance

$$\xi(\mathbf{k}, t) = p_{\mathrm{f}}\sqrt{2k_{\mathrm{B}}TL(\mathbf{k})\Delta t}\,\mu(\mathbf{r}, t) \quad (16)$$

where Δt is the time step increment. The coefficient, p_{f}, is a constant which is introduced as a correction factor that takes into account the fact that the correlation equations have been derived from linearized kinetic equations which are strictly valid only at infinitely high temperatures, and the current simulations are being performed using a non-linear kinetic equation at finite temperatures [30]. It also serves to ensure that the noise term does not become too large, so that numerical stability can be maintained. In this work, the focus is on coarsening kinetics, so the noise terms were introduced entirely for the purpose of nucleating ordered particles when the parent disordered phase is metastable.

3. THE THERMODYNAMIC MODEL

In this paper, a two-neighbor interaction model is assumed for the Al–Li system and the values for the interaction parameters W_1 and W_2 are 40.435 and −31.59 meV, respectively [1, 27]. The variation of the interatomic interaction parameters with composition was ignored. The low-temperature part of the $\alpha + \delta'$ two-phase field using these interaction parameters is reproduced in Fig. 2, in which the dot-dashed line (T_-) represents the ordering instability line below which a disordered phase is absolutely unstable with respect to ordering, the thin solid line (T_o) is the locus along which the ordered and disordered phases have the same free energy, the dashed line (T_+) is the disordering instability line above which an ordered phase is absolutely unstable with respect to disordering, and the thick solid lines are equilibrium phase boundaries. The free energy curves for the ordered and disordered phases as a function of composition at $T = 192°\mathrm{C}$ are shown in Fig. 3. According to Figs 2 and 3, at this temperature the equilibrium composition (of Li in atomic or mole fraction) of the disordered phase (α), C_α, is ∼0.068; the equilibrium composition of the metastable ordered phase δ', $C_{\delta'}$, is ∼0.223; the composition at which the disordered phase becomes absolutely unstable with respect to δ' ordering, or the ordering instability composition, C_-, is ∼0.131; the composition at which the δ' ordered phase is absolutely unstable with respect to disordering, C_+, is ∼0.106; and the composition at

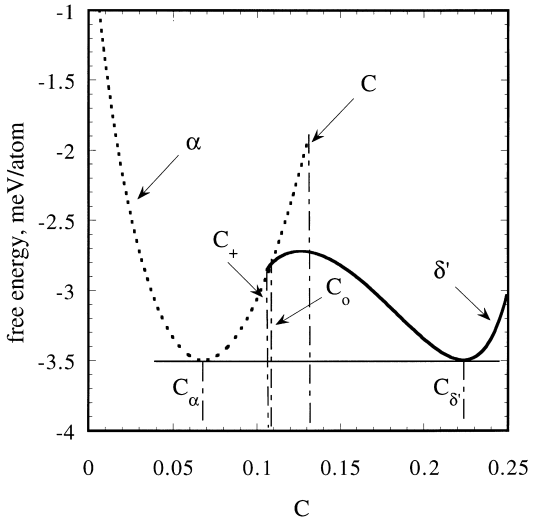

Fig. 3. The free energy vs composition curves at $T = 192°\mathrm{C}$. The labels are explained in the text.

which the ordered and disordered phases have the same free energy, C_o, is ~0.109.

Based on the interaction parameters, a value of 0.0166 J/m^2 at $T = 192°C$ was obtained for the interfacial energy between the δ' precipitates and the disordered matrix along the ⟨1, 0, 0⟩ directions. In the calculation, both the ordered and disordered phases are assumed to have the equilibrium compositions. Since the interfacial energy along the ⟨1, 0, 0⟩ direction is the lowest, this value represents the minimum interfacial energy. However, at finite temperatures, the interfacial energy anistropy is small, and hence it is expected that this value is a good approximation. The value, 0.0166 J/m^2, is in good agreement with an early experimentally reported value of 0.014 J/m^2 [32], but is significantly higher than a more recently obtained value of 0.005 J/m^2 both experimentally [33] and theoretically using first-principle calculations [34]. It should be emphasized that the main conclusions of the paper on the volume-fraction dependencies of PSDs, scaled structure functions, and coarsening rate constants, are not affected by the exact values of the interfacial energy, although the absolute value of the coarsening rate constant are roughly proportional to the magnitude of interfacial energy.

4. RELATION OF MICROSCOPIC AND CONTINUUM DIFFUSION EQUATIONS

In order to compare the simulation results with experimental measurements and analytical theories, the kinetic parameter employed in the microscopic model needs to be related to the phenomenological diffusion coefficient in the continuum model. To accomplish this, the relation between the microscopic and continuum diffusion equations is considered in the disordered state. In the disordered state, the solution to equation (4), $\tilde{P}(\mathbf{k},t)$, has significant values only around $\mathbf{k} = 0$, with $|\mathbf{k}|$ of the order of $2\pi/d$, where d is a typical size of composition domains, i.e. $\tilde{P}(\mathbf{k},t)$ at small $\mathbf{k}$ is the Fourier transform of the macroscopic composition profile, $C(\mathbf{r})$. At small k, the $\tilde{L}(k)$ function can be expanded as [23, 35]

$$\tilde{L}(\mathbf{k}) = \tilde{L}(0) + \left(\frac{\partial \tilde{L}(\mathbf{k})}{\partial k_i}\right)_{\mathbf{k}=0} k_i + \frac{1}{2}\left(\frac{\partial^2 \tilde{L}(\mathbf{k})}{\partial k_i \partial k_j}\right)_{\mathbf{k}=0} k_i k_j + \cdots \quad (17)$$

where $\tilde{L}(0)$ is the value of $\tilde{L}(\mathbf{k})$ at $k = 0$, which is zero from the conservation condition for the total number of solute atoms. In the expansion (17), the Einstein summation convention is invoked. The second term in equation (17) is zero by symmetry consideration. Therefore, the first nonvanishing term for $\tilde{L}(\mathbf{k})$ at k close to 0 is the third term

$$\tilde{L}(\mathbf{k}) = -M_{ij} k_i k_j \quad (18)$$

where

$$M = -\frac{1}{2}\left(\frac{\partial^2 \tilde{L}(\mathbf{k})}{\partial k_i \partial k_j}\right)_{\mathbf{k}=0}.$$

Substituting equation (18) into equation (6) and ignoring the noise term, gives

$$\frac{\mathrm{d}\tilde{P}(\mathbf{k}, t)}{\mathrm{d}t} = -\frac{MC_o(1 - C_o)k_i k_j}{k_B T}\left(\frac{\delta F}{\delta P(\mathbf{r}, t)}\right)_{\mathbf{k}}. \quad (19)$$

Its Fourier original

$$\frac{\mathrm{d}\tilde{P}(\mathbf{r}, t)}{\mathrm{d}t} = \frac{MC_o(1 - C_o)}{k_B T}\nabla_i \nabla_j \left(\frac{\delta F}{\delta P(\mathbf{r}, t)}\right) \quad (20)$$

is the real space macroscopic Cahn–Hilliard equation [36] for the composition profile since for the disordered state, the single-site occupation probability function, $P(\mathbf{r},t)$, is the same as the local composition, $C(\mathbf{r},t)$. For an isotropic system, it is

$$\frac{\partial C(\mathbf{r}, t)}{\partial t} = \frac{MC_o(1 - C_o)}{k_B T}\nabla^2 \left(\frac{\delta F}{\delta C(\mathbf{r}, t)}\right). \quad (21)$$

Therefore, the expansion constant M can be related to the chemical diffusion coefficient through

$$D = \frac{MC_o(1 - C_o)}{k_B T}\left(\frac{\partial^2 f(C)}{\partial C^2}\right)_{C=C_\alpha} \quad (22)$$

where C_α is the composition of the disordered matrix. In equation (22), the mean field free energy per lattice site for the disordered matrix phase is given by [27]

$$f(C) = \frac{1}{2}(12W_1 + 6W_2)C^2 + k_B T\left[C \ln C + (1 - C)\ln(1 - C)\right] \quad (23)$$

where W_1, W_2 are first- and second-neighbor effective interchange energies, C the solute composition, k_B the Boltzmann constant, and T the temperature. Therefore

$$D = \frac{MC_o(1-C_o)}{k_B T}\left(12W_1 + 6W_2 + \frac{k_B T}{C_\alpha(1 - C_\alpha)}\right). \quad (24)$$

Using equation (12) for $\tilde{L}(\mathbf{k})$, M is given by

$$M = -\frac{1}{2}\left(\frac{\partial^2 \tilde{L}(\mathbf{k})}{\partial k_i \partial k_j}\right)_{\mathbf{k}=0} = L_1 a_o^2 \quad (25)$$

where L_1 is the nearest-neighbor jump probability given in equation (12) and a_o the lattice parameter of the f.c.c. lattice. Therefore, in terms of the phenomenological chemical diffusion coefficient, L_1 in the microscopic model is given by

Table 1. Alloy compositions and corresponding volume fractions investigated in this study

Li composition in atomic fraction	Equilibrium volume fraction of δ' phase (%)	Volume fraction derived from the simulation (%)
0.10	20.5	20.1
0.12	33.3	33.1
0.135	42.9	42.9
0.15	52.6	52.3
0.17	65.4	65.2

$$L_1 = \frac{Dk_BT}{C_o(1-C_o)a_o^2\left(12W_1+6W_2+\frac{k_BT}{C_\alpha(1-C_\alpha)}\right)}. \quad (26)$$

5. RESULTS AND DISCUSSION

Computer simulations were performed for several representative compositions within the $\alpha + \delta'$ two-phase field labeled by small circles in the phase diagram at $T = 192°C$ (Fig. 2). They are listed in Table 1 together with the corresponding equilibrium volume fractions of the δ' phase. The last column in Table 1 represents the volume fractions determined from the asymptotic dependence of volume fraction on time during coarsening obtained from the simulations as it will be discussed later.

In the simulation, reduced time, given by $t^* = tL_1$, was employed. According to expression (26), L_1 is a function of overall composition, C_o. However, for convenience

$$C_o(1 - C_o)/k_BT = 1/680 \text{ (meV)}$$

in the kinetic equation (6) and in equation (26) for all the compositions, which merely results in a rescaling of the time. Using equation (26) with $D = 6.47 \times 10^{-15}$ cm^2/s, $a_o = 4 \times 10^{-8}$ cm [37, 38], the interaction parameters described in the last section, and $C_o(1 - C_o)/k_BT = 1/680$ (meV), $L_1 = 2.95$/s is obtained. The time step size is $\Delta t^* = 0.005$ for all the compositions.

System sizes with 512×512 and 1024×1024 lattice points were employed. For all compositions, the initial condition for the single-site occupation probability function corresponds to the completely disordered phase, which was obtained by assigning the average composition to occupation probabilities at each lattice point, plus a small random noise. For $C_{Li} = 0.10$ and 0.12, the initial disordered state is metastable and hence a noise term is added to provide a sufficient number of critical nuclei of δ' phase particles. Since the nucleation and growth rates of precipitate are of no interest here, the same noise distribution was added at each time step for the initial 1000 time steps for $C_{Li} = 0.10$ and 0.12. The value used for p_f in equation (16) is 0.01. During the subsequent growth and coarsening, the noise term was removed. For $C_{Li} = 0.135$, 0.15, and 0.17, the initial disordered state is unstable with respect to $L1_2$ ordering and therefore the initial random perturbation is sufficient to initiate ordering and precipitation of $L1_2$ ordered domains. However, in previous work, it was shown that with the thermal noise term included, the size of the congruently ordered domains is smaller, and hence the number of particles is larger, compared to that obtained without the thermal noise [1]. Therefore, for these compositions, the same noise distribution was also kept on for the initial 1000 time steps to increase the number of particles in the system.

5.1. Morphological evolution

Figure 4 shows an example of microstructural evolution for $C_{Li} = 0.10$ obtained using 512×512 lattice points. The gray-levels in Fig. 3 represent the local compositions, with white representing high values and black representing low values. The local compositions were calculated by locally averaging occupation probabilities over nearest- and next-nearest neighbor sites. In this representation, the white particles in Fig. 3 are ordered δ' particles and black is the disordered matrix. Coalescence between two close-up particles may or may not take place,

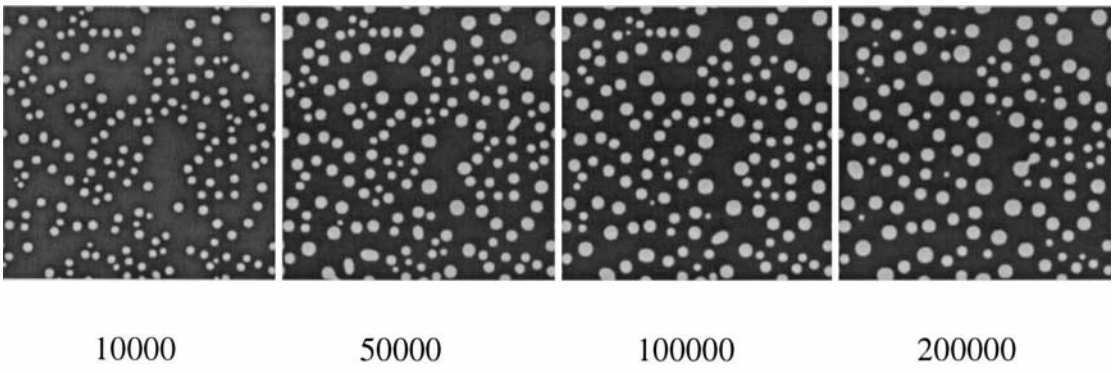

Fig. 4. Snap-shots of δ' precipitate morphologies in an Al–Li alloy with $C_{Li} = 0.10$ at four different time steps during a computer simulation using 512×512 lattice points.

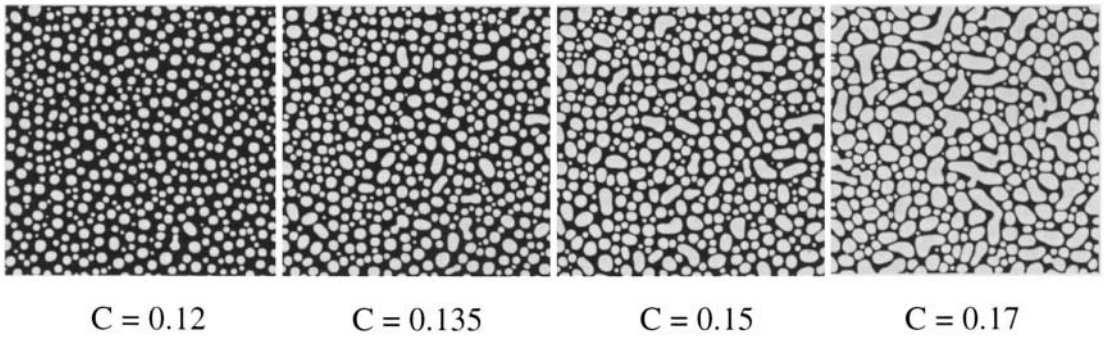

Fig. 5. Morphologies of δ' precipitates as a function of composition or volume fraction obtained by computer simulations using 1024×1024 lattice points.

depending on whether or not they belong to the same kind of antiphase domains. For this composition, the volume fraction is relatively low, so the coalescence event is rare. The dumbbell particle at time step 200,000 is a result of coalescence. It can also be seen that some close-by particles, separated by the disordered phase, remain separated until the smaller ones finally dissolve. As expected, during the coarsening process, large particles grow and small particles disappear as a function of time, with the volume fraction of the δ' phase approximately constant. The two-phase microstructures as a function of volume fraction obtained using 1024×1024 lattice points are shown in Fig. 5. Although the interfacial energy is nearly isotropic, the shape of the particles becomes increasingly non-spherical as the volume fraction of precipitates increases (Fig. 5). The predicted volume fraction dependence of the two-phase morphology is in excellent agreement with that observed by Mahalingam *et al.* [15].

5.2. Structure function analysis

It has been shown that a two-phase morphology during coarsening can be characterized by a time-dependent structure function [39–43]. Following Ref. [43], the structure function is defined as

$$S(\mathbf{k}, t) = \frac{1}{N}\left\langle \sum_{\mathbf{r}} \sum_{\mathbf{r}'} \left[C(\mathbf{r}' + \mathbf{r}, t) C(\mathbf{r}', t) - C_{\mathrm{o}}^2 \right] \mathrm{e}^{-\mathrm{i}\mathbf{k}\mathbf{r}} \right\rangle \tag{27}$$

where N is the total number of lattice points, $C(\mathbf{r})$ the local composition, and C_{o} the overall composition. By performing a "circular" averaging of the structure function

$$S(k, t) = \frac{\sum_{k-\Delta k/2<|\mathbf{k}|<k+\Delta k/2} S(\mathbf{k}, t)}{\sum_{k-\Delta k/2<|\mathbf{k}|<k+\Delta k/2} 1} \tag{28}$$

where $k = |\mathbf{k}|$. The normalized structure function is defined as

$$s(k, t) = \frac{S(k, t)}{\sum_{\mathbf{k}} S(\mathbf{k}, t)} = \frac{S(k, t)}{N\left[\langle C^2(\mathbf{r})\rangle - C_{\mathrm{o}}^2\right]} \tag{29}$$

where angular brackets denote averaging over all lattice points.

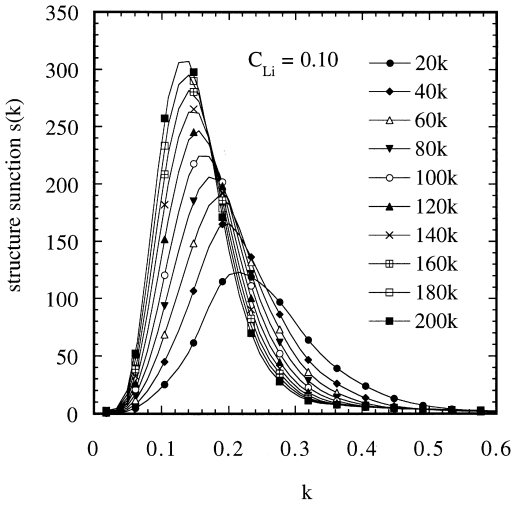

Fig. 6. Structure functions as a function of k at ten different time steps for $C_{\mathrm{Li}} = 0.10$.

Figure 6 shows an example of the normalized and circularly averaged structure function $s(k,t)$ at ten different time steps for composition $C_{\mathrm{Li}} = 0.10$ obtained using a 1024×1024 lattice simulation. The lines are spline fits to the simulation data. As expected, with increasing time, the maximum value of the structure function increases and shifts to lower k, indicating an increase in the real-space average precipitate length scale.

The typical length scale, $\langle R\rangle$, which corresponds to the average δ' particle size, can be characterized by either $\langle R\rangle^{-1} \sim k_{\max}(t)$, the position of the maximum in $s(k,t)$, or $k_1(t)$, the first moment of the structure function [41], with the nth moment of $s(k,t)$ being defined as

$$k_n(t) = \frac{\sum k^n s(k, t)}{\sum s(k, t)}. \tag{30}$$

It was found more convenient to define the typical length scale as the inverse of the first moment of $s(k,t)$, because the position of the maximum in

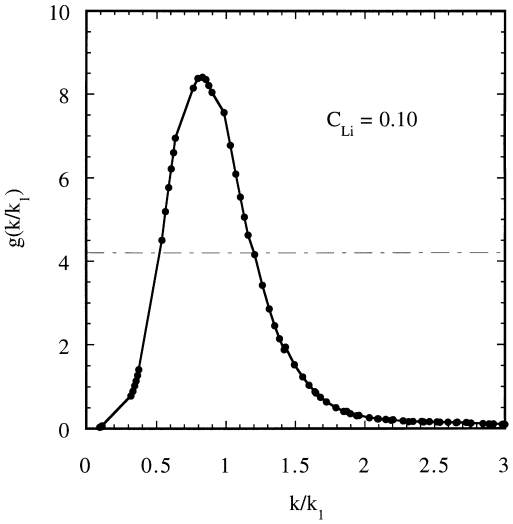

Fig. 7. Scaling function as a function of k/k_1 obtained from six time steps at late stages of coarsening for $C_{Li}=0.10$.

$s(k,t)$ cannot be very precisely determined and it depends on the resolution with which $s(k,t)$ is measured. With this definition of the typical length scale, the scaling function $g(kR)$ is [42]

$$g(kR, t) = g(k/k_1; t) = k_1^2(t)s(k, t). \qquad (31)$$

If the structure function does indeed scale, then $g(k/k_1; t) = g(k/k_1)$ is expected.

The scaling function for $C_{Li}=0.10$ collected from six different times, but represented with the same markers, is shown in Fig. 7. It can be seen that the data points from different times fall on the same master curve, indicating that the scaling regime had been attained. k_1 in Fig. 7 is the first moment of k as defined in equation (30). The scaling function obtained from this simulation was compared with that obtained by Che *et al.* for the Al–9.3% Li alloy at 130°C [45] in Fig. 8. For the simulation, the data in Fig. 7 were renormalized using k_{max} (the k value at which the structure function is a maximum) for k and g_{max} (the maximum value for the structure function) for $g(k/k_1)$; for the experimental results, the data points were obtained by examining Fig. 4 in Ref. [45] using human eyes, and the values for the structure function were also normalized by its maximum. It is rather surprising that except for a few data points in the small k region, the agreement between the experimentally measured scaling function and that obtained in the present simulation is excellent.

Table 2. Full width at half maximum of the scaling function of volume fraction obtained from the simulation

Equilibrium volume fraction (%)	Full width at half maximum
20.5	0.83
33.3	0.75
42.9	0.73
52.6	0.74
65.4	0.77

The volume fraction dependence of the scaling function was also investigated. The full width at half maximum of the scaling functions obtained from different volume fractions are listed in Table 2. It should be pointed out that there is a difference in the values for the full width at half maximum, depending on whether the first moment of the structure function or the maximum position is used as the measure of the inverse of the typical length scale of the two-phase morphology. In order to compare with data obtained from other sources, the data given in Table 2 were renormalized using k_{max} although the initial scaling functions were obtained using the first moment as the measure for the length scale. The data points of Fig. 5 from Ref. [45] were

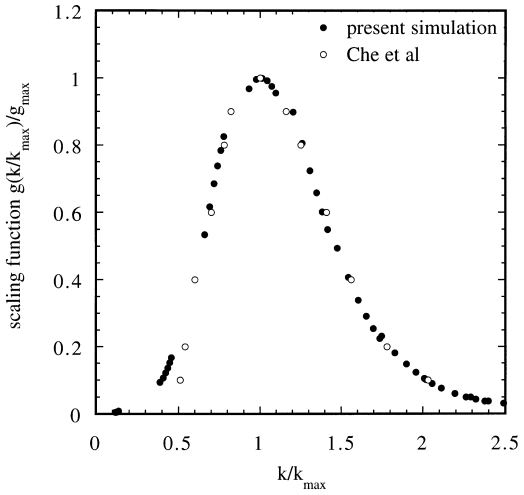

Fig. 8. Comparison of scaling functions obtained from experiments by Che *et al.* [45] and the present simulation by normalizing the scaling function using its maximum value and k using k_{max}.

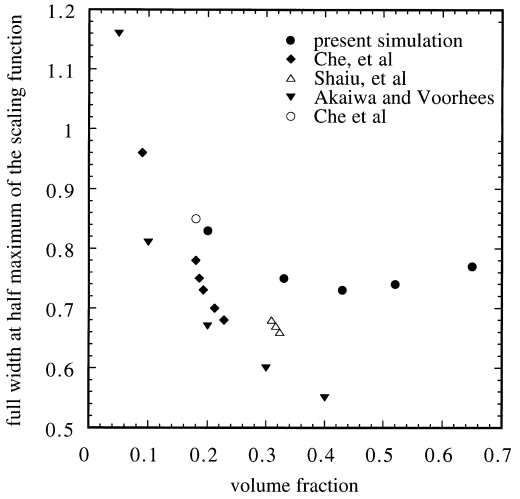

Fig. 9. Full width at half maximum of scaled structure function as a function of volume fraction adapted from Fig. 5 of Ref. [45]. The open circle represents the datum estimated from Fig. 4 of Ref. [45].

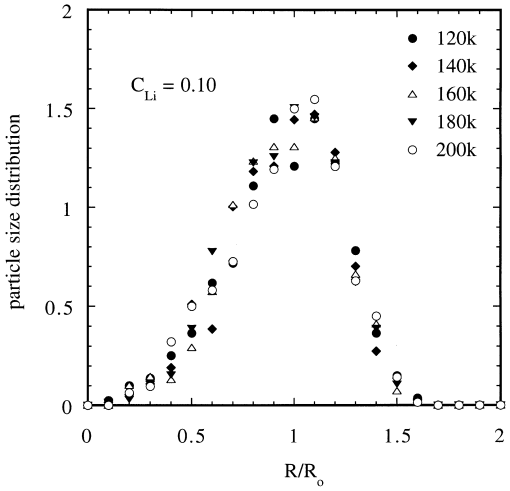

Fig. 10. Particle size distributions at five different time steps for $C_{Li}=0.10$.

re-plotted in Fig. 9 with the simulation results included as solid circles. The open circle labeled as "Che *et al.*" is the data point estimated from Fig. 4 of Ref. [45] by using the same type of estimate as in the present simulation, which has an excellent agreement with the simulation results as it should be based on Fig. 8. It may be noted that the present simulation results show a systematic increase in the full width of half maximum beyond 50% volume fraction. According to Fig. 9, the experimental data points by both Che *et al.* [45] and Shaiu *et al.* [46] fall in between those obtained in the present quasi-2D simulation and those obtained by Akaiwa and Voorhees using a sharp-interface continuum model in 3D.

5.3. Particle size distributions (PSDs)

PSDs were obtained from simulations using a system size of 1024×1024 lattice points. The size of a precipitate was determined by counting the total number of lattice points within a particle at which the local composition is larger than $(C_\alpha + C_{\delta'})/2$, and hence the unit of the size is $a_o/2$ (the lattice parameter of the projected 2D square lattice) where a_o is the lattice parameter of the original 3D f.c.c. lattice. The averaged relative frequency curves (where the frequency within an interval is assigned to the center of the interval) are shown in Fig. 10 for the composition $C_{Li}=0.10$. There were about 600 particles left after 200,000 time steps. The distributions were found to be approximately independent of time, indicating that the steady state regime had been reached. The coefficient of size variation (which is the ratio of the standard deviation to the mean) was relatively constant for the time steps shown in Fig. 10, which also implies that steady state had been attained.

A statistical analysis of the distributions for each volume fraction was performed and the data on the skewness are shown in Fig. 11. According to Fig. 11, the skewness changes sign from negative to positive as volume fraction increases, becoming zero at about 0.40 volume fraction. A comparison of the PSDs for $C_{Li}=0.10$ and 0.17 is given in Fig. 12. The lines are drawn by hand as a guide to the human eye (note that the long tail is towards the left for $C_{Li}=0.10$ and towards the right for $C_{Li}=0.17$ in Fig. 12). It is also shown that the PSD for $C_{Li}=0.17$ is broader than that for $C_{Li}=0.10$. As a matter of fact, the PSDs systematically broaden and the maximum values for the PSD systematically decrease as volume fraction increases, consistent with several theoretical and experimental results. For $C_{Li}=0.10$, the maximum particle radius is approximately 1.6 times the average size, very close to that predicted by the original LSW theory. On the other hand, the cutoff in particle sizes occurs at $\sim$2.5 times $\langle R \rangle$ for $C_{Li}=0.17$.

Although the simulations were performed in a projected 2D system and the LSEM theory is developed for 3D systems, the fact that there is a change

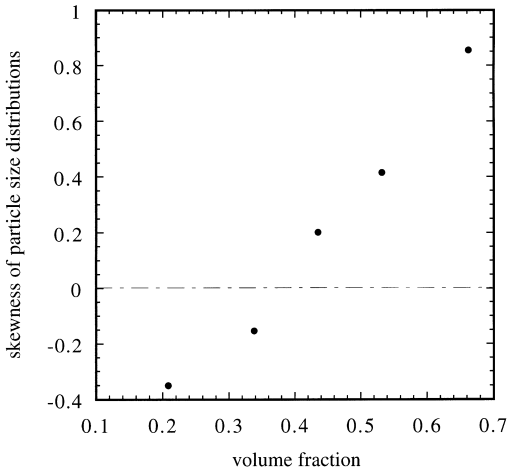

Fig. 11. The variation of skewness of the particle size distributions with volume fraction.

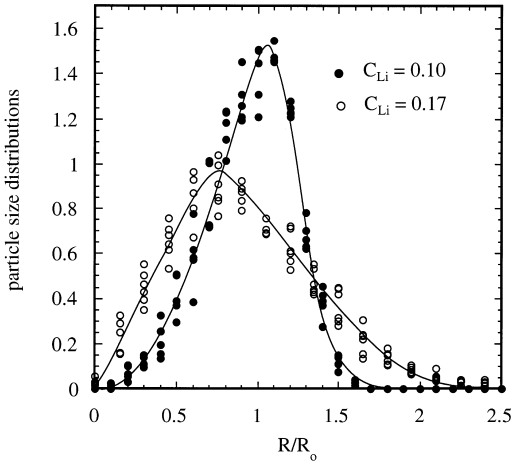

Fig. 12. Comparison of particle size distributions at two different compositions or volume fractions.

of sign in the skewness of the PSDs as a function of volume fraction obtained in the simulation, is consistent with the LSEM theory and other experimental studies on this system: Mahalingam *et al.* [15] reported a change from negative to positive at a volume fraction between 0.27 and 0.46, while Kamio and Sato [17] reported a skewness close to zero at a volume fraction of 0.30. The only theoretical models which predict this change in skewness are the LSEM model [14], and the recently reported Brailsford Wynblatt encounter modified (BWEM) model [47]. The LSEM model takes into account the fact that during coarsening, two particles may coalesce, which changes the size distribution in such a way as to take two particles out of the smaller size ranges, and put one particle into the larger size range. This leads to broader PSDs than those predicted by Lifshitz and Slyozov [2], as well as to a change in the skewness of the distribution from negative to positive at a volume fraction of about 0.40–0.45. However, none of the existing theories have taken into account the effect of antiphase domains on the probability of coalescence. The LSEM model assumes that any two particles that meet will coalesce. For the $L1_2$ ordered phase, however, there is a 75% probability that two particles will be in antiphase relation, and will not coalesce. It has been suggested [47] that this can be taken into account by multiplying the "encounter integral" of the LSEM model by 0.25. However, this implies that the PSD curves of the LSEM model that were earlier valid for a volume fraction $Q = 0.8$, will now be valid for $Q = 0.2$. This changes all the predictions of the LSEM model with regard to the volume fraction at which the skewness becomes zero (0.4–0.45) and other statistical measures.

Since the simulations were performed in a projected 2D system, it is relevant to discuss some of the existing 2D theories and simulation studies. A study of two of the most widely quoted 2D theoretical models [48, 49] and all previous 2D computer simulations shows that none of them predict the observed change in skewness as a function of volume fraction. However, at low volume fractions, the PSDs obtained from the simulations are very similar to those obtained earlier by Akaiwa and Meiron [18] and Chakrabarti *et al.* [43]. Akaiwa and Meiron used a sharp interface model for their simulations and did not take into account the particle coalescence while Chakrabarti *et al.* employed the Cahn–Hilliard equation which takes into account coalescence but did not distinguish different antiphase domains.

5.4. Kinetics of coarsening

Essentially all existing theories and experimental evidence demonstrated that the cube of the average precipitate particle size during coarsening of second-phase particles is linearly proportional to time

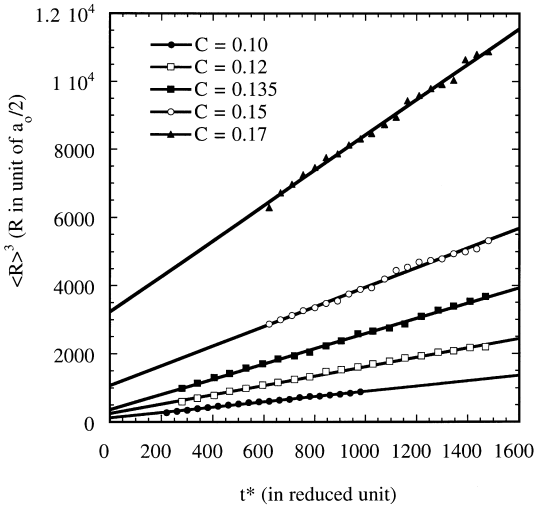

Fig. 13. The cube of the average size as a function of time for different compositions. The units for t^* and R are explained in the text.

in the scaling regime, i.e.

$$\langle R\rangle^3 - R_o^3 = Kt \tag{32}$$

where $\langle R\rangle$ is the average radius at a given time, R_o the initial average particle size at $t = 0$, and K the rate constant for coarsening.

The variations of the cube of average particle size with time obtained from the computer simulations are shown in Fig. 13 for the five compositions studied. The size of the domains was calculated in real space by a brute force technique that counted the number of lattice points within a given domain. The average radius of domains was then taken to be proportional to the square root of the average area. It can be seen that the cube of average size varies with time approximately linearly for all the volume fractions studied. Straight lines are linear fits at different volume fractions. There is a systematic increase in the slopes of the lines as the composition or volume fraction increases.

By converting the length unit (in $a_o/2$) to real unit and time steps or reduced time t^* to real time [related by L_1 in equation (26)], the rate constants obtained from the slopes of linear fits in Fig. 13 for different volume fractions were listed in Table 3. In agreement with previous theories and experimental observations, rate constant increases with volume fraction. The rate constant as a function of volume fraction is plotted in Fig. 14 along with the predic-

Table 3. Rate constant as a function of volume fraction obtained from the simulation

Equilibrium volume fraction (%)	Rate constant (10^{-29} m^3/s)
20.5	1.84
33.3	3.24
42.9	5.28
52.6	6.82
65.4	12.27

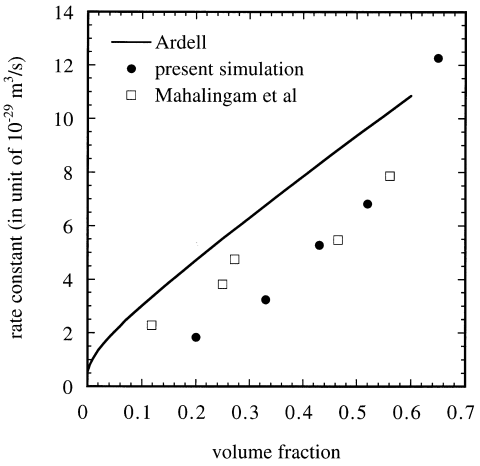

Fig. 14. Comparison of rate constants obtained in the present simulation with those predicted by Ardell's two-dimensional theory [49] and experimental results by Mahalingam *et al.* [15].

tion from Ardell's theory [49] in cylindrical coordinates and the experimental measurements by Mahalingam *et al.* in Al–Li alloys [15]. The rate constant in Ardell's theory [49], modified based on the work of Calderon *et al.* [50], is given by

$$K = \frac{3L^{\alpha}D}{(C_{\delta'} - C_{\alpha})}\frac{\langle u\rangle^3}{\zeta} \tag{33}$$

where D is the diffusion coefficient, $C_{\delta'}$ and C_{α} the equilibrium compositions of the precipitate phase and the matrix, respectively, $\langle u\rangle$ a constant of order of magnitude unity given by the ratio of average particle radius to the critical particle radius of the LSW theory, ξ is also a constant dependent on volume fractions. Both $\langle u\rangle$ and ξ are tabulated in Ref. [49]. L^{α} in equation (33) is a capillary length given by [50]

$$l^{\alpha} = \frac{V_{\delta'}\sigma}{\left(\partial^2 f/\partial C^2\right)|_{C=C_{\alpha}}(C_{\delta'} - C_{\alpha})} \tag{34}$$

where σ is the interfacial energy, f the free energy of the solid solution per lattice site given in equation (23), and $V_{\delta'}$ the volume of the precipitate phase per lattice site.

The rate constant values for Ardell's theory in Fig. 14 were obtained by using the diffusion coefficient which was used to fit the kinetic coefficient L_1, the interfacial energy calculated based on the interchange energies, the values of the second derivatives of the free energy expression (23) evaluated at the equilibrium composition of the disordered phase, and the equilibrium compositions of the precipitate and matrix from the phase diagram in Fig. 2. Since the free energy was evaluated per lattice site of the projected square lattice, the volume per lattice site is given by $(a_o/2)^3$ (area per lattice site $\times$ lattice spacing of the (001) plane), where a_o is the original f.c.c. lattice parameter. It is shown in Fig. 14 that the rate constants predicted by Ardell's theory are consistently higher than those obtained in the present simulation except for a volume fraction of 0.65 at which Ardell's theory is not expected to be valid any longer. It can be noticed in Fig. 14 that the variation of rate constant with volume fraction obtained from the simulation has a positive curvature whereas Ardell's theory predicted a negative curvature. Interestingly, similar (positively curved) dependence of the rate constant on volume fraction to the simulated results was obtained by Mahalingam *et al.* [15] in Al–Li alloys at 225°C, and also predicted by the recent statistical coarsening theory by Marsh and Glicksman [13]. The experimental data included in Fig. 14 by Mahalingam *et al.* [15] were obtained at 200°C which is closer to the simulation temperature, which shows approximately linear dependence of rate constant on volume fraction. The rate constants predicted from the simulations show very good agreement with those measured by Mahalingam *et al.* [15], which might be accidental considering the fact the rate constant depends on the specific values of both the diffusion coefficient and the interfacial energy.

5.5. Volume fraction dependence on time

As pointed out by Ardell [4], the volume fraction of the precipitate phase is not a constant and approaches the equilibrium value only asymptotically. To derive the asymptote, the overall supersaturation of solute atoms during coarsening is written as

$$C_{\alpha} - C_{\alpha,e} = \frac{l^{\alpha}}{R^*} = \frac{\langle u\rangle l^{\alpha}}{\langle R\rangle} \tag{35}$$

where C_{α} is the average composition of the matrix at a given time, R^* the critical particle size at which the particle growth rate is zero, $\langle u\rangle$ a constant of order of magnitude unity as in equation (33), and L^{α} a capillary length given by equation (34). To distinguish the equilibrium composition from the average composition of the matrix, in equation (35) and the following equations, $C_{\alpha,e}$ is used to denote the equilibrium composition.

If $\langle R\rangle$ is much larger than R_o in equation (32), the variation of supersaturation as a function of time can be expressed as [51]

$$C_{\alpha} - C_{\alpha,e} = (\kappa t)^{-1/3} \tag{36}$$

where the constant κ is given by

$$\kappa = \frac{K}{\langle u\rangle^3\left(l^{\alpha}\right)^3}. \tag{37}$$

The volume fraction of precipitate phase, Q, at any given time is then given by the lever rule as

$$Q = \frac{C_o - C_{\alpha}}{C_{\delta'} - C_{\alpha}} = \frac{C_o - C_{\alpha,e} - (\kappa t)^{-1/3}}{C_{\delta'} - C_{\alpha,e} - (\kappa t)^{-1/3}} \tag{38}$$

where C_o is the overall composition of the alloy, $C_{\delta'}$

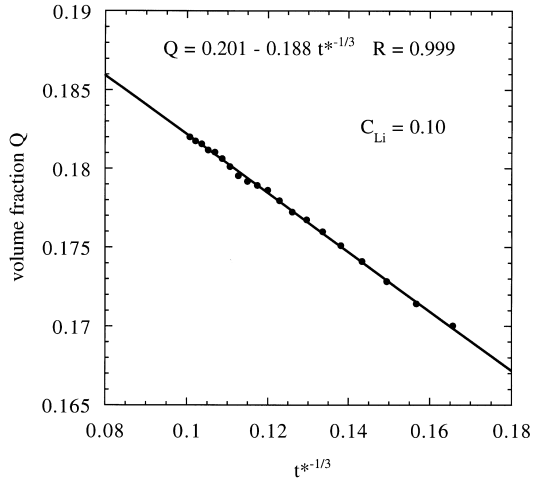

Fig. 15. Volume fraction as a function of $t^{*-1/3}$ during coarsening in the system with $C_{\mathrm{Li}}=10$.

the equilibrium composition of the ordered phase. By expanding the denominator in equation (38) and ignoring higher order terms

$$Q = Q_{\mathrm{e}} - \frac{(1-Q_{\mathrm{e}})}{C_{\delta'} - C_{\alpha,\mathrm{e}}}(\kappa t)^{-1/3} \tag{39}$$

which shows that the volume fraction, Q, approaches its equilibrium value Q_{e} asymptotically with time as $t^{-1/3}$. Therefore, by plotting Q vs $t^{-1/3}$, the constant, κ, can be determined from the slope and the equilibrium volume fraction, Q_{e}, from the y-intercept. Figure 15 shows such a plot for composition $C_{\mathrm{Li}}=0.10$. From the linear fit, the intercept, $\sim$0.201, is the equilibrium volume fraction. Figure 16 shows the same plot for all the compositions studied. The equilibrium volume fractions obtained in this way are listed in Table 1 in the third column. The volume fractions determined in this analysis are very close to those calculated from the equilibrium phase diagram (the second column in Table 1).

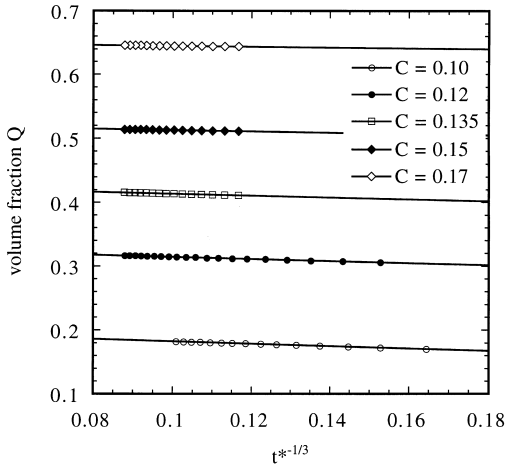

Fig. 16. Volume fraction as a function of $t^{*-1/3}$ during coarsening for different compositions.

With the two rate constants, K and κ, the capillary length is given by [51] [from equation (37)]

$$l^{\alpha} = \left(\frac{K}{\kappa}\right)^{1/3} \Big/ \langle u \rangle. \tag{40}$$

For example, for $C_{\mathrm{Li}}=0.10$, $K = 1.84\times10^{-29}$ m^3/s, $\kappa = 6.05\times10^{4}$/s (from Fig. 15 and then convert its reduced unit to a real unit), and using the value 1.0 for $\langle u \rangle$, the capillary length is 6.7×10^{-12} m. With the capillary length and the thermodynamic model [equation (23)], equation (34) can be used to calculate the interfacial energy. Using the coarsening data for $C_{\mathrm{Li}}=0.10$, a value can be obtained for the interfacial energy, 0.0195 J/m^2. Compared to the value calculated for the (001) interfacial energy, 0.0166 J/m^2, directly from the interchange energies and the mean-field model (8), the value obtained from the coarsening data is about 20% larger. This difference may be due to a number of reasons. First of all, the value 0.0166 J/m^2 was calculated for a planar (001) interface which has the lowest interfacial energy. Moreover, both precipitate and disordered phase were assumed to have the equilibrium compositions, which is not the case during coarsening. However, the overall agreement in the interfacial energies values obtained from the two different approaches is quite good. Therefore, as suggested by Ardell, quite a reliable interfacial energy value can be extracted based on reliable coarsening data [51]. Furthermore, if there is a coarsening theory to link the rate constant K and the diffusion coefficient as well as the interfacial energy or the capillary length, it may be possible to back-calculate the diffusion coefficient based on the coarsening data, e.g. using expression (33).

6. CONCLUSION

This paper reports a computer simulation study of the kinetics of coarsening of the δ' particles in binary Al–Li alloys. It is found that the morphologies of the δ' precipitates become increasingly non spherical and the frequency of coalescence increases as the volume fraction increases. For all the volume fractions studied, it is shown that $\langle R \rangle^3 \sim t$ kinetics is obeyed in the scaling regime while the rate constant increases with volume fraction. Quantitative values for the kinetic coefficients and the interfacial energy are all in good agreement with available experimental measurements. It is demonstrated that the PSDs become increasingly broad and the skewness of the PSDs changes from negative to positive with increasing volume fraction, consistent with experimental evidence in this system. The scaling function calculated for $\sim$20% volume fraction also shows good agreement with recent experimental measurement in an alloy with similar composition. The volume fraction was found to approach the equilibrium value asymptotically.

Acknowledgements—The authors are grateful for the useful discussions with A.J. Ardell and J.J. Hoyt. The work is supported by ONR under grant number N-00014-95-1-0577, the DARPA/NIST program on mathematical modeling of microstructure evolution in advanced alloys, and NSF under grant number DMR 96-33719. Computation time was provided through a grant of HPC time from the DoD HPC center, CEWES, on the C90, and a grant from Pittsburgh Supercomputing Center.

REFERENCES

1. Poduri, R. and Chen, L.-Q., *Acta mater*., 1997, **45**, 245.
2. Lifshitz, I. M. and Slyozov, V. V., *J. Phys. Chem. Solids*, 1961, **19**, 35.
3. Wagner, C., *Z. Elektrochem*., 1961, **65**, 681.
4. Ardell, A. J., *Phase Transformations '87*, The Institute of Metals, London, 1987, p. 485, Ardell, A. J., in *The Mechanism of Phase Transformations in Crystalline Solids*, 33, The Institute of Metals, London, 1969, p. 111.
5. Tsumuraya, K. and Miyata, Y., *Acta metall*., 1983, **31**, 437.
6. Asimov, R., *Acta metall*., 1963, **20**, 61.
7. Sarian, S. and Weart, H. W., *J. Appl. Phys*., 1969, **37**, 1675.
8. Aubauer, H. P., *J. Phys. F: Metal Phys*., 1978, **8**, 375.
9. Brailsford, A. D. and Wynblatt, P., *Acta metall*., 1979, **27**, 489.
10. Voorhees, P. W. and Glicksman, M. E., *Acta metall*., 1984, **32**, 2013.
11. Marqusee, J. A. and Ross, J., *J. Chem. Phys*., 1984, **80**, 536.
12. Tokyuama, M. and Kawasaki, K., *Physica*, 1984, **123A**, 386.
13. Marsh, S. P. and Glicksman, M. E., *Acta mater*., 1996, **44**, 3761.
14. Davies, C. K. L., Nash, P. and Stevens, R. N., *Acta metall*., 1980, **28**, 179.
15. Mahalingam, K., Gu, B. P., Liedl, G. L. and Sanders, T. H., *Acta metall*., 1987, **35**, 483.
16. Ardell, A. J., *Acta metall*., 1972, **20**, 61.
17. Kamio, A. and Sato, T., *Report of the Research Group for Study of Phase Separation in Al–Li Based Alloys*, Light Metal Education Foundation, Osaka, Japan, 1993.
18. Akaiwa, N. and Meiron, D. I., *Phys. Rev*., 1996, **E54**, R13.
19. Khachaturyan, A. G., *Theory of Structural Transformations in Solids*, Wiley, New York, 1983.
20. Chen, L. Q. and Khachaturyan, A. G., *Acta metall. mater*., 1991, **39**, 2533.
21. Wang, Y., Chen, L. Q. and Khachaturyan, A. G., *Acta metall. mater*., 1994, **41**, 279.
22. Chen, L. Q., Wang, Y. and Khachaturyan, A. G., *Phil. Mag. Lett*., 1992, **64**, 241.
23. Wang, Y., Chen, L. Q. and Khachaturyan, A. G., in *Computer Simulation in Materials Science—Nano/Meso/Macroscopic Space and Time Scales*, ed. H. O. Kirchner *et al*.. NATO ASI Series, Kluwer Academic, Dordrecht, 1996, p. 325.
24. Chen, L. Q. and Wang, Y., *JOM*, 1996, 13 Dec.
25. Wang, Y. and Khachaturyan, A. G., *Acta mater*., (accepted).
26. Li, D. Y. and Chen, L. Q., *Scr. mater*., 1997, **37**, 1271.
27. Poduri, R. and Chen, L. Q., *Acta mater*., 1996, **44**, 4253.
28. Shang, Keng Ma, *Modern Theory of Critical Phenomena*, W.A. Benjamin, Reading, Massachusetts, 1976.
29. Cook, H. E., *Acta metall*., 1970, **18**, 297.
30. Khachaturyan, A. G., Wang, Y. and Wang, H. Y., *Materials Science Forum*, 1994, **155**(156), 345.
31. Khachaturyan, A. G., Lindsey, T. F. and Morris, J. W., *Metall. Trans*., 1988, **19A**, 249.
32. Baumann, S. F. and Williams, D. B., *Scr. metall*., 1984, **18**, 611.
33. Hoyt, J. J. and Spooner, S., *Acta metall. mater*., 1991, **39**, 689.
34. Asta, M., *Acta mater*., 1996, **44**, 4131.
35. Chen, L. Q., *Mod. Phys. Lett*., 1993, **B7**, 1857.
36. Cahn, J. W., *Acta metall*., 1961, **9**, 795.
37. Sato, T. and Kamio, A., *Mater. Trans. Jap. Inst. Metals*, 1990, **31**, 25.
38. Yu, M.-S. and Chen, H. H., in *Report of the Research Group for Study of Phase Separation in Al–Li Based Alloys*. Light Metal Education Foundation, Osaka, Japan, 1993, p. 45.
39. Binder, K., Billotet, C. and Mirold, P., *Z. Phys*., 1978, **B30**, 313.
40. Furukawa, H., *Phys. Rev. Lett*., 1979, **43**, 136.
41. Lebowitz, J. L., Marro, J. and Kalos, M. H., *Acta metall*., 1982, **30**, 297.
42. Yeomans, J., in *Solid → Solid Phase Transformations*, ed. W. C. Johnson *et al*. TMS-AIME, 1994, p. 189.
43. Chakrabarti, A., Toral, R. and Gunton, J. D., *Phys. Rev. E*, 1993, **47**, 3025.
44. Gunton, J. D., San Miguel, M. and Sahni, P. S., in *Phase Transitions and Critical Phenomena*, **8**, ed. C. Domb and J. L. Lebowitz, 1983, p. 267.
45. Che, D. Z., Spooner, S. and Hoyt, J. J., *Acta mater*., 1997, **45**, 1167.
46. Shaiu, B. J., Li, H. T., Lee, H. Y. and Chen, H., *Metall. Trans*., 1990, **A21**, 1133.
47. Jayanth, C. S. and Nash, P., *J. Mater. Sci*., 1989, **24**, 3041.
48. Marqusee, J., *J. Chem. Phys*., 1984, **81**, 976.
49. Ardell, A. J., *Phys. Rev. B*, 1990, **41**, 2554.
50. Calderon, H. A., Voorhees, P. W., Murray, J. L. and Kostorz, G., *Acta metall. mater*., 1994, **42**, 991.
51. Ardell, A. J., *Interface Science*, 1995, **3**, 119.